Study on two-dimensional mixed-mode fatigue crack growth employing ordinary state-based peridynamics

Hanlin Wang[a], Satoyuki Tanaka[a,*], Selda Oterkus[b], Erkan Oterkus[b]

[a] *Graduate School of Advanced Science and Engineering,*
Hiroshima University, Japan,
e-mail: hanlinwang@hiroshima-u.ac.jp,
satoyuki@hiroshima-u.ac.jp
[b] *Department of Naval Architecture, Ocean and Marine Engineering,*
University of Strathclyde, United Kingdom,
e-mail: selda.oterkus@strath.ac.uk,
erkan.oterkus@strath.ac.uk

Abstract

Mixed-mode fatigue crack propagation analysis is studied using ordinary state-based peridynamics. By introducing the concept of “remaining life”, the fatigue crack nucleation and propagation can be simulated in the PD framework. The PD fatigue modeling and the crack path prediction is carefully investigated. For the comparison purpose, the maximum circumferential stress criterion is introduced. The interaction integral and the peridynamic differential operator is employed to evaluate the fracture mechanics parameters. Two pre-cracked structures under mixed-mode loading conditions are provided with the validations from reference solutions.

Keywords: Fatigue crack growth, Peridynamics, Fracture mechanics, Maximum circumferential stress criterion, Meshfree method

---

1. Introduction

Structural safety has always been an issue of high concern in the marine industry. Among the many type of marine structural failures, the fatigue is commonly regarded as one of the major failure modes for ships and offshore facilities. These structures, generally, are connected by weld joints, where

---

[*] Corresponding author

high stresses are likely concentrated [1]. Under cyclic loadings by waves, winds or even severe conditions, fatigue damage might gradually accumulate in the weld joints, and contribute to the emergence of crack and failure on the structure, leading to catastrophic accident eventually. Therefore, the fatigue fracture analysis is of vital importance in the marine design, assessment and maintenance.

Even though the mechanism behind the fatigue failure is not fully understood till today [2], there still many efforts were devoted to the relevant investigations. Based on the experimental observation of aluminium plates, Paris et al. [3] had established the relationship between crack growth rate and range of stress intensity factor (SIF). This pioneering finding had provided a useful and reliable theoretical support for the damage tolerance evaluation in many research fields.

With the improvement of computing performance, many numerical methods were developed into the fatigue crack growth analysis. Sander and Richard [4] conducted a two-dimensional (2D) mixed-mode fatigue failure experiment, finding out the retardation effect on fatigue crack growth rate and crack path deflection. Then by using finite element method (FEM), they further explored the causes of the retardation under different mixed-mode loading conditions in detail. Nguyen et al. [5] introduced the cohesive model into the FEM to resolve the near-tip plastic fields using adaptive meshing to predict the fatigue life. Yan and Nguyen-Dang [6] utilized the dual boundary element method to simulate multiple crack fatigue problem. Singh et al. [7] employed the extended FEM to investigate the influence of different type discontinuities on fatigue life. Based on FEM, crack propagation approach was also proposed to describe the relationship between load cycles and fatigue crack growth [8-10].

Since cracks and damages are geometrically discontinuous, the partial differential equations, which are widely employed in the mesh-based numerical methods, might become hindrance in the fracture analysis. Re-meshing process is necessary during the simulation, negatively affecting the efficiency and accuracy of the numerical solutions [11-13]. Therefore, many meshfree approaches were developed. Duflot and Nguyen-Dang [14] proposed a meshfree method by introducing an enriched weight function. By accurately evaluating the SIFs, the growth of multiple fatigue cracks were predicted. Jameel and Harmain [15] predicted the crack growth and evaluated the fatigue life of the structures with inclusion and hole by using element free Galerkin method (EFGM) [16]. Pathak et al. [17] investigated the 3D fatigue crack behaviours under thermo-elastic loadings by coupling the FEM and EFGM. Dai et al. [18] analyzed the fatigue crack propagation on cylindrical shell by using reproducing kernel particle method (RKPM) [19-21].

In recent years, peridynamic (PD) theory was proposed for the fracture analysis [22], and it has many applications in several fracture problems [23,24]. Oterkus et al. [25] proposed a novel fatigue model in predicting the crack growth. The bond stretch in this model consist of elastic and plastic part. Meanwhile, the critical stretch will decrease as the number of load cycle increase. Therefore, it could simulate the fatigue damages caused by the plastic deformation. Silling and Askari [26] introduced the concept of "remaining life" to the bond kinematics. In considering the S-N curve and Paris law [3,27], the fatigue crack initiation and propagation can be respectively simulated. Based on Silling's model [26], Nguyen et al. [28] developed a novel bond breakage criterion for the fatigue model. The fatigue crack growth was determined by cyclic bond energy release rate. Jung and Seok [29] had extended the Silling's model by taking the mixed-mode loading condition into consideration, and successfully applied in the fatigue crack growth analysis of heterogeneous material [30]. There are also many researches and applications of the PD fatigue model, which can be found in the literature [31-33].

Even though there are many studies about the prediction of fatigue crack growth by using PD in the literature, an in-depth investigation is still necessary. Therefore, several 2D model with pre-existed crack will be tested in this study. The interaction integral, originally proposed by Yau et al. [34], will be reformulated based on the PD framework and utilized in the calculation of SIFs. Meanwhile, the crack growth based on maximum circumferential stress (MCS) criterion, proposed by Erdogan and Sih [35], will also be examined as a comparison with the PD fatigue model. The bond-based PD (BPD), as originally proposed by Silling [22,36], is an over simplified model, which have some limitations on material properties. Poisson's ratio is constant as 1/3 and 1/4 for 2D and 3D problems, respectively. Therefore, it is not suitable for simulations considering plastic deformation. Hence, Silling [37] modified the BPD model and proposed ordinary state-based peridynamics (OSPD) by introducing the concept of "state".

In this study, mixed-mode fracture analysis on 2D problems are provided based on the OSPD. Both original PD fatigue model and PD MCS model will be demonstrated and compared in detail. Therefore, in the second section, the concept of OSPD and the corresponding PD fatigue model will be briefly illustrated. The meshfree interaction integral method is addressed in the third section. Then, mixed-mode numerical studies are presented in the fourth section to validate the PD fatigue model. Finally, some major findings of this research are discussed and concluded in the final sections.

2. 2D Ordinary state-based peridynamics

PD is firstly introduced by Silling [22] as an alternative approach of solid mechanical modeling. As a nonlocal theory, PD has taken long range interactions into consideration, which is fundamentally different from classical continuum mechanics (CCM) [38]. In numerical modelling of PD, structures are discretized by finite number of material points accompanied with volumes in space without meshing. Therefore, it has superiority in the fracture analysis. As shown in Fig. 1, material point could build up interactions with its neighbour points within certain distance, named as “Horizon” (H_x). The interaction between each pair of points is known as “bond”, where pairwise force might arise after deformation. The horizon size is denoted as δ. In this study, δ is selected as 3 times of grid space by considering the numerical accuracy and computational efficiency.

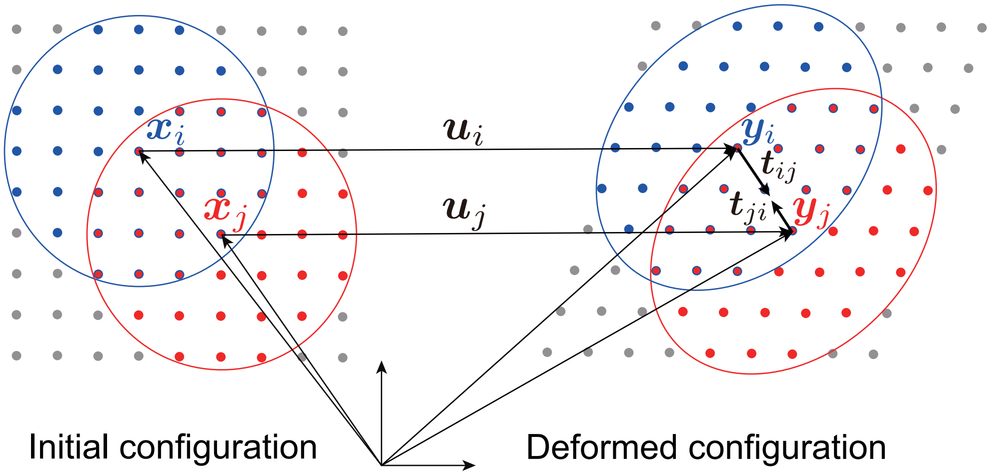

Figure 1: Kinematics in OSPD.

2.1. Equation of motion

Different from CCM, the motion of a material point in PD can be described by an integral equation as:

$$\rho \ddot{\boldsymbol{u}}_i = \int_{H_x} \{\boldsymbol{t}_{ij}(\boldsymbol{u}_i, \boldsymbol{u}_j, \boldsymbol{x}_i, \boldsymbol{x}_j, t) - \boldsymbol{t}_{ji}(\boldsymbol{u}_i, \boldsymbol{u}_j, \boldsymbol{x}_i, \boldsymbol{x}_j, t)\} dV_j + \boldsymbol{b}_i(t), \tag{1}$$

where ρ refers to the mass density of a point. $\boldsymbol{x}_i$ and $\boldsymbol{x}_j$ are the position vector of points i and j, respectively, in the initial configuration. $\boldsymbol{u}_i$ and $\boldsymbol{u}_j$ represent the displacement vectors. $\boldsymbol{t}_{ij}$ and $\boldsymbol{t}_{ji}$ are the pairwise force vectors of points as shown in Fig. 1. $\boldsymbol{b}_i(t)$ refers to the body force density subjected to the point i at time t. The volume of point j is denoted as V_j.

In the numerical implementation of Eq. (1), V_j on the horizon boundary might not be fully enclosed due to the disk shape of the horizon. Therefore, some correction factors added on the volume is necessary to ensure the accuracy of the numerical simulation. The pairwise force densities are derived from the strain energy density, which consists of the dilatation and distortion terms as:

$$W = a_1 \theta_i^2 + b \int_{H_x} \omega_{ij} (|\boldsymbol{y}_j - \boldsymbol{y}_i| - |\boldsymbol{x}_j - \boldsymbol{x}_i|)^2 dV_j, \tag{2}$$

where $\boldsymbol{y}_i$ and $\boldsymbol{y}_j$ refer to the position vectors on bond in the deform configuration. θ_i is the dilatation term for point i, which can be expressed as:

$$\theta_i = d \int_{H_x} \omega_{ij} s_{ij} \frac{\boldsymbol{y}_j - \boldsymbol{y}_i}{|\boldsymbol{y}_j - \boldsymbol{y}_i|} \cdot (\boldsymbol{x}_j - \boldsymbol{x}_i) dV_j, \tag{3}$$

where ω_{ij} and s_{ij} are weight function and stretch for a bond. ω_{ij} is manually defined, which controls the strength of the interactions between points on a bond. Usually, the farther distance between the points, the weaker the bond. In this article, the bond stretch and weight function are respectively defined as:

$$\omega_{ij} = \frac{\delta}{|\boldsymbol{x}_j - \boldsymbol{x}_i|}, \quad s_{ij} = \frac{|\boldsymbol{y}_j - \boldsymbol{y}_i| - |\boldsymbol{x}_j - \boldsymbol{x}_i|}{|\boldsymbol{x}_j - \boldsymbol{x}_i|}. \tag{4}$$

a_1, b and d in Eqs. (2) and (3) are PD parameters. For 2D analysis, they can be expressed as:

$$a_1 = \frac{\lambda\alpha - \mu}{2}, \quad b = \frac{6\mu}{\pi h \delta^4}, \quad d = \frac{2}{\pi h \delta^3}, \tag{5}$$

where h represents thickness of the 2D structure. Lamé's constant, λ and μ, and coefficient α are expressed as:

$$\lambda = \frac{E\nu}{(1+\nu)(1-2\nu)}, \quad \mu = \frac{E}{2(1+\nu)}, \tag{6a}$$

$$\alpha = \begin{cases} (1-2\nu)/(1-\nu) & \text{for plane stress} \\ 1 & \text{for plane strain} \end{cases}. \tag{6b}$$

Therefore, the pairwise bond force density $\boldsymbol{t}_{ij}$ can be determined from the spatial partial differentiation of W, which can be expressed as:

$$\begin{aligned} \boldsymbol{t}_{ij} &= \frac{1}{V_j}\frac{\partial W}{\partial(|\boldsymbol{y}_j - \boldsymbol{y}_i|)}\frac{\boldsymbol{y}_j - \boldsymbol{y}_i}{|\boldsymbol{y}_j - \boldsymbol{y}_i|} \\ &= 2a_1 d \cdot \omega_{ij}\theta_i\Lambda_{ij}\frac{\boldsymbol{y}_j - \boldsymbol{y}_i}{|\boldsymbol{y}_j - \boldsymbol{y}_i|} + 2b \cdot \omega_{ij}(|\boldsymbol{y}_j - \boldsymbol{y}_i| - |\boldsymbol{x}_j - \boldsymbol{x}_i|)\frac{\boldsymbol{y}_j - \boldsymbol{y}_i}{|\boldsymbol{y}_j - \boldsymbol{y}_i|}, \end{aligned} \tag{7}$$

where Λ_{ij} can be expressed as:

$$\Lambda_{ij} = \frac{\boldsymbol{y}_j - \boldsymbol{y}_i}{|\boldsymbol{y}_j - \boldsymbol{y}_i|} \cdot \frac{\boldsymbol{x}_j - \boldsymbol{x}_i}{|\boldsymbol{x}_j - \boldsymbol{x}_i|}. \tag{8}$$

Substituting Eq. (7) to Eq. (1), the motion of material points could be determined.

2.2. Static solution

Even though Eq. (1) is in the dynamic form, it can still be applied in static analysis. Kilic and Madenci [39] introduced adaptive dynamic relaxation (ADR) technique, which is derived from the theory proposed by Underwood [40]. By manually introducing damping modulus into the dynamic formed equation of motion, the numerical solutions could converge into static values. ADR is an explicit method, but it does not have limitations on time step size [38]. Moreover, it does not require high computing performance. Therefore, it is convenient to be implemented in PD.

However, in some special problems without sufficient boundary constraints, it will take relatively long computing time for structures to reach a steady state. Meanwhile, for quasi-static analysis with crack growth, the damping factors might need to be modified as the crack propagating in order to get a good computing efficiency. In this manner, the ADR, perhaps, is not suitable in the simulation of fatigue crack growth, since it requires large amount of computational time.

Apart from ADR, the static solution can also be calculated by setting $\rho\ddot{\boldsymbol{u}}_i$ in Eq. (1) to 0. Then, Eq. (1) can be numerically reformulated as:

$$\sum\nolimits_{H_x}[\boldsymbol{t}_{ij}(\boldsymbol{u}_i,\boldsymbol{u}_j,\boldsymbol{x}_i,\boldsymbol{x}_j,t)-\boldsymbol{t}_{ji}(\boldsymbol{u}_i,\boldsymbol{u}_j,\boldsymbol{x}_i,\boldsymbol{x}_j,t)]V_j=-\boldsymbol{b}_i(t), \tag{9}$$

where $\sum_{H_x}$ refers to the summation within the horizon. Then, substituting Eq. (7), Eq. (9) can be rewritten as:

$$\sum\nolimits_{H_x}2\omega_{ij}\{a_1d(\theta_i+\theta_j)\Lambda_{ij}+2b(|\boldsymbol{y}_j-\boldsymbol{y}_i|-|\boldsymbol{x}_j-\boldsymbol{x}_i|)\}\frac{\boldsymbol{y}_j-\boldsymbol{y}_i}{|\boldsymbol{y}_j-\boldsymbol{y}_i|}V_j=-\boldsymbol{b}_i(t). \tag{10}$$

The bond stretch s_{ij} in Eq. (4) represents the elongation or shortening of a bond. It can also be reformulated as:

$$s_{ij}=\frac{(u_j-u_i)e^1_{ij}+(v_j-v_i)e^2_{ij}}{|\boldsymbol{\xi}|}, \tag{11}$$

where u_i and u_j are displacements along x-direction of points i and j, respectively. Similarly, v_i and v_j refer to the displacements along y-direction. The bond length $|\boldsymbol{\xi}|$ can be expressed by $|\boldsymbol{x}_j$-$\boldsymbol{x}_i|$. e^1_{ij}=cosφ and e^2_{ij}=sinφ respectively express the x- and y-components of unit vector along the bond. φ is the angle between bond and x-axis. Therefore, the dilatation term, Eq. (3), can be numerically rewritten as:

$$\theta_i=d\sum\nolimits_{H_x}\omega_{ij}\Lambda_{ij}V_j\begin{bmatrix}-e^1_{ij} & -e^2_{ij} & e^1_{ij} & n^2_{ij}\end{bmatrix}\cdot\begin{bmatrix}u_i & v_i & u_j & v_j\end{bmatrix}^T=\boldsymbol{k}^\theta_i\cdot\boldsymbol{u}^L, \tag{12}$$

where $\boldsymbol{k}^\theta_i$ is the coefficient matrix of θ_i with 1×2n in size. $\boldsymbol{u}^L$ is the displacement vector in terms of point i and all its neighbour points with 2n×1 in size. They can be expressed as:

$$\boldsymbol{k}^\theta_i=d\begin{bmatrix}\text{elem1} & \text{elem2} & c_1\Lambda_{ij}e^1_{ij_1} & c_1\Lambda_{ij}e^2_{ij_1} & ... & c_n\Lambda_{ij}e^1_{ij_n} & c_n\Lambda_{ij}e^2_{ij_n}\end{bmatrix}, \tag{13a}$$

$$\boldsymbol{u}^L=\begin{bmatrix}u_i & v_i & u_{j_1} & v_{j_1} & ... & u_{j_n} & v_{j_n}\end{bmatrix}^T, \tag{13b}$$

where the coefficients c_1 and c_n refer to $\omega_{ij_1}V_{j_1}$ and $\omega_{ij_n}V_{j_n}$, respectively. The elements in Eq. (13a), elem1 and elem2, can be expressed as:

$$\text{elem1}=-\sum\nolimits_{H_x}\omega_{ij}\Lambda_{ij}e^1_{ij}V_j,\quad \text{elem2}=-\sum\nolimits_{H_x}\omega_{ij}\Lambda_{ij}e^2_{ij}V_j. \tag{14}$$

Therefore, for global structure, the dilatation term can be expressed as:

$$\begin{aligned}\boldsymbol{\Theta} &= \begin{bmatrix}\theta_1 & \theta_2 & ... & \theta_N\end{bmatrix}^T \\ &= \begin{bmatrix}\boldsymbol{k}_1^\theta & \boldsymbol{k}_2^\theta & ... & \boldsymbol{k}_N^\theta\end{bmatrix}^T \cdot \begin{bmatrix}u_1 & v_1 & u_2 & v_2 & ... & u_N & v_N\end{bmatrix}^T \\ &= \boldsymbol{K}^\theta \cdot \boldsymbol{U}^T,\end{aligned} \tag{15}$$

where $\boldsymbol{K}^\theta$ is the global coefficient matrix of dilatation with the size of $N \times 2N$. Besides, $\boldsymbol{U}$ refers to the global displacement vector with the size of $1 \times 2N$. N is the total number of material points in the structure.

According to Eqs. (1) and (7), the resultant force on one point can be decomposed into two terms, which can be expressed as:

$$\begin{aligned}\sum\nolimits_{H_x}(\boldsymbol{t}_{ij} - \boldsymbol{t}_{ji})V_j = 2a_1 d \sum\nolimits_{H_x} \omega_{ij}\Lambda_{ij}(\theta_i + \theta_j)\begin{bmatrix}e_{ij}^1 & e_{ij}^2\end{bmatrix}^T V_j \\ + 4b\sum\nolimits_{H_x}\omega_{ij}\left[(u_j - u_i)e_{ij}^1 + (v_j - v_i)e_{ij}^2\right]\begin{bmatrix}e_{ij}^1 & e_{ij}^2\end{bmatrix}^T V_j.\end{aligned} \tag{16}$$

The first term of right hand side of Eq. (16) is named as "Term 1" and the second term is denoted as "Term 2". Hence, the Term 1 can be reformulated as:

$$\begin{aligned}\text{Term 1} &= 2a_1 d \sum\nolimits_{H_x}\omega_{ij}\Lambda_{ij}V_j\begin{bmatrix}e_{ij}^1 & e_{ij}^1 \\ e_{ij}^2 & e_{ij}^2\end{bmatrix} \cdot \begin{bmatrix}\theta_i & \theta_j\end{bmatrix}^T \\ &= \boldsymbol{k}_i^{dila} \cdot \begin{bmatrix}\theta_i & \theta_1 & ... & \theta_n\end{bmatrix}^T,\end{aligned} \tag{17}$$

where the local coefficient matrix for this term, $\boldsymbol{k}_i^{dila}$, can be expressed as:

$$\boldsymbol{k}_i^{dila} = 2a_1 d\begin{bmatrix}\sum_{H_x}\omega_{ij}\Lambda_{ij}e_{ij}^1 V_j & c_1\Lambda_{ij}e_{ij_1}^1 & ... & c_n\Lambda_{ij}e_{ij_n}^1 \\ \sum_{H_x}\omega_{ij}\Lambda_{ij}e_{ij}^2 V_j & c_1\Lambda_{ij}e_{ij_1}^2 & ... & c_n\Lambda_{ij}e_{ij_n}^2\end{bmatrix}. \tag{18}$$

Therefore, for all points in global scale, the first term in the pairwise force density can be expressed as:

$$\text{Term 1} = \boldsymbol{K}^{dila} \cdot \boldsymbol{\Theta} = \boldsymbol{K}^{dila} \cdot \boldsymbol{K}^\theta \cdot \boldsymbol{U}^T, \tag{19}$$

where the $\boldsymbol{K}^{dila}$ is the collection of corresponding local coefficient matrix in a matrix with a size of $2N \times N$, which can be written as:

$$\boldsymbol{K}^{dila} = \begin{bmatrix}\boldsymbol{k}_1^{dila} & \boldsymbol{k}_2^{dila} & ... & \boldsymbol{k}_N^{dila}\end{bmatrix}^T. \tag{20}$$

On the other hand, the second term corresponding to distortion, can be locally expressed as:

$$\begin{aligned}\text{Term 2} &= 4b\sum\nolimits_{H_x}\omega_{ij}V_j\begin{bmatrix}-(e_{ij}^1)^2 & -e_{ij}^1e_{ij}^2 & (e_{ij}^1)^2 & e_{ij}^1e_{ij}^2\\ -e_{ij}^1e_{ij}^2 & -(e_{ij}^2)^2 & e_{ij}^1e_{ij}^2 & (e_{ij}^2)^2\end{bmatrix}\cdot\begin{bmatrix}u_i & v_i & u_j & v_j\end{bmatrix}^T\\ &= \boldsymbol{k}_i^{dist}\cdot\boldsymbol{u}^L,\end{aligned} \tag{21}$$

where the local coefficient matrix for the second term, $\boldsymbol{k}_i^{dist}$ can be expressed as:

$$\boldsymbol{k}_i^{dist} = 4b\begin{bmatrix}\text{elem3} & \text{elem4} & c_1(e_{ij_1}^1)^2 & c_1e_{ij_1}^1e_{ij_1}^2 & \ldots & c_n(e_{ij_n}^1)^2 & c_ne_{ij_n}^1e_{ij_n}^2\\ \text{elem4} & \text{elem5} & c_1e_{ij_1}^1e_{ij_1}^2 & c_1(e_{ij_1}^2)^2 & \ldots & c_ne_{ij_n}^1n_{ij_n}^2 & c_n(e_{ij_n}^2)^2\end{bmatrix}, \tag{22}$$

where the elements, elem3, elem4 and elem5, can be respectively expressed as:

$$\begin{aligned}&\text{elem3} = -\sum\nolimits_{H_x}\omega_{ij}(e_{ij}^1)^2V_j,\quad \text{elem4} = -\sum\nolimits_{H_x}\omega_{ij}e_{ij}^1e_{ij}^2V_j,\\ &\text{elem5} = -\sum\nolimits_{H_x}\omega_{ij}(e_{ij}^2)^2V_j.\end{aligned} \tag{23}$$

Therefore, for all points in global scale, the second term in the pairwise force density can be expressed as:

$$\text{Term 2} = \boldsymbol{K}^{dist}\cdot\boldsymbol{U}^T, \tag{24}$$

where the $\boldsymbol{K}^{dist}$ is the collection of corresponding local coefficient matrix in a matrix with a size of $2N\times2N$, which can be written as:

$$\boldsymbol{K}^{dist} = \begin{bmatrix}\boldsymbol{k}_1^{dist} & \boldsymbol{k}_2^{dist} & \ldots & \boldsymbol{k}_N^{dist}\end{bmatrix}^T. \tag{25}$$

Hence, by reformulating the Eq. (7) in terms of Eqs. (19) and (24), and then substituting back to Eq. (9), the relationship between displacements and loadings can be established as:

$$-\left[\boldsymbol{K}^{dila}\cdot\boldsymbol{K}^{\theta}+\boldsymbol{K}^{dist}\right]\cdot\boldsymbol{U}^T = \boldsymbol{K}\cdot\boldsymbol{U}^T = \boldsymbol{b}, \tag{26}$$

where $\boldsymbol{K}$ can be regarded as the global stiffness matrix of the structure based on the generalized Hooke's law, and the loading vector $\boldsymbol{b}$, with the size of $2N\times1$ can be expressed as:

$$\boldsymbol{b} = \begin{bmatrix}b_1^x & b_1^y & b_2^x & b_2^y & \ldots & b_N^x & b_N^y\end{bmatrix}^T, \tag{27}$$

where b_i^x and b_i^y are x- and y-components of loading. Then, by multiplying inverse of the stiffness matrix, the displacement field of the structure can be determined as:

$$\boldsymbol{U}^T = \boldsymbol{K}^{-1}\cdot\boldsymbol{b}. \tag{28}$$

2.3. Peridynamic fatigue model

In original PD framework, once the bond stretch exceeds a critical value, s_c, bond will irreversibly break as shown in Fig. 2. As the percentage of broken bond increasing, crack nucleation and propagation can be observed. However, cracks and damages can still gradually accumulate in a body under cyclic loadings even though the critical bond stretch, s_c, is not met. In order to simulate this fatigue damage, Silling and Askari [26] proposed a PD fatigue model by introducing a concept of "remaining life" for the bond. The decay of the remaining life depends on the cyclic strain range, ϵ, which is provided as:

$$\epsilon = |\epsilon^+ - \epsilon^-| = |\epsilon^+(1 - R)|, \tag{29}$$

where ϵ^+ and ϵ^- are bond stretch at maximum and minimum loadings, respectively. It could also be expressed by the load ratio, R, which is the ratio between maximum and minimum loadings. With the increase of load cycle, N_L, the remaining life, λ_f, will decrease. Once, the λ_f reduces below 0, then bond will break, and the fatigue damage emerges. The remaining life decay can be expressed as:

$$\frac{d\lambda_f(N_L)}{dN_L} = -A(\epsilon - \epsilon_{th})^m, \tag{30}$$

where ϵ_{th} refers to the threshold cyclic bond stretch, which is the minimum value that will lead to the remaining life decay.

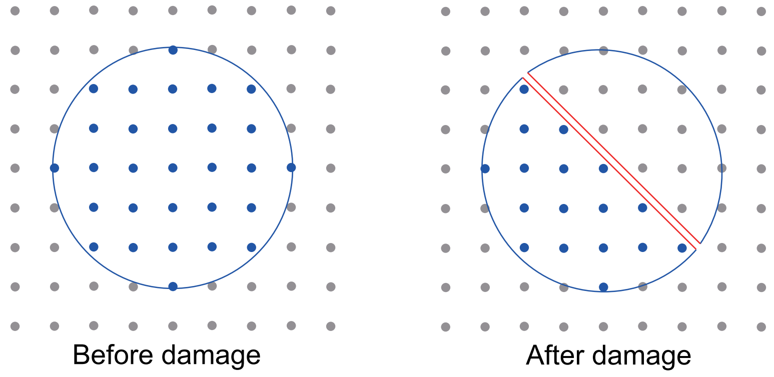

Figure 2: Damage for a material point within its horizon.

In PD fatigue model, crack nucleation, stable crack growth and unstable crack propagation are respectively defined as Phase I, II and III. A and m are parameters, which depend on different phases. For crack nucleation, the remaining life decay in a single cycle without considering the threshold bond stretch can be numerically expressed as:

$$\lambda_f(N_L) = \lambda_f(N_L - 1) - A_1 \epsilon^{m_1}, \tag{31}$$

where A_1 and m_1 are fatigue parameters in Phase I. Eq. (31) gives the relationship between bond remaining life on current and last cycles. Considering the remaining life just reaches 0 at cycle N_1, the bond will break in the next cycle. In this manner, $A_1 \epsilon^{m_1} N_1$=1. Reconstructing in logarithmic scale as $\log N_1$=-$\log A_1$-$m_1 \log \epsilon$, a linear relationship can be derived as shown in Fig. 3. Then the parameters A_1 and m_1 can be determined respectively.

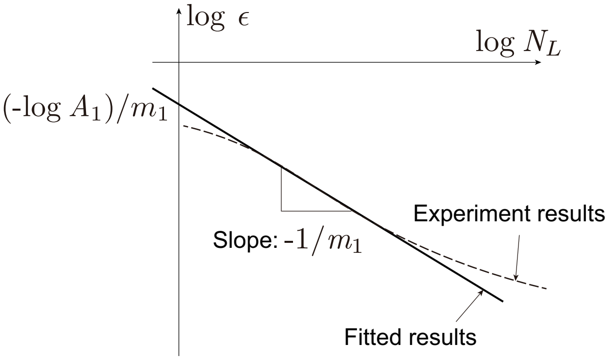

Figure 3: S-N curve derived from experiment.

For Phase II, the remaining life reduction in a single cycle without considering the threshold bond stretch can be numerically expressed as:

$$\lambda_f(N_L) = \lambda_f(N_L - 1) - A_2 \epsilon^{m_2}, \tag{32}$$

where parameters, A_2 and m_2, can be calculated according to Paris law [3], which is expressed as:

$$\frac{da}{dN_L} = \bar{C} \Delta K^{\bar{m}}, \tag{33}$$

where a refers to the crack length. ΔK represents the range of SIFs. $\bar{C}$ and $\bar{m}$ are fitting parameters which can be derived from experimental data of the material. In order to better describe the fatigue crack growth, Silling and Askari [26] introduced a local coordinate system always originated at the crack tip, as shown in Fig. 4. The relationship between global and local coordinates are given as:

$$x_l = x - \frac{da}{dN_L} N_L, \tag{34}$$

where x_l and y_l are axes of local coordinate system. For bond on the crack tip, which is called "critical bond", the λ_f will reach 0 for the first time during cyclic loadings. For bond on the edge of horizon, λ_f=1.

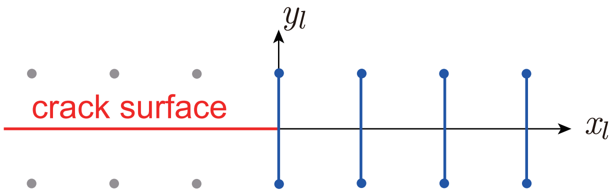

Figure 4: Bonds ahead of crack tip.

As crack grows, the bond on the horizon edge will move to the crack tip. At the same time, the remaining life will gradually decrease and eventually break. This process can be represented by an integration as:

$$\lambda_f(x_l = 1) = \lambda_f(x_l = 0) + \int_0^\delta \frac{d\lambda_f}{dx_l} dx_l. \tag{35}$$

Substituting Eq. (30) without considering ϵ_{th} to Eq. (35), the crack growth rate can be reformulated as:

$$\frac{da}{dN_L} = A_2 \int_0^\delta \epsilon^{m_2} dx_l. \tag{36}$$

According to [26], based on the mode-I assumption, the stretch of bond in the vicinity of the crack tip can be expressed as:

$$\epsilon(x_l) = \epsilon(0)\hat{f}, \tag{37}$$

where $\hat{f}$ is relevant to the material property and position. Therefore, Eq. (36) can be rewritten as:

$$\frac{da}{dN_L} = A_2(\epsilon(0))^{m_2} \int_0^\delta \hat{f}^{m_2} dx_l = A_2(\epsilon(0))^{m_2}\beta. \tag{38}$$

Hence, by comparing Eq. (38) with Eq. (33), the relationship of m_2=$\bar{m}$ is confirmed, while the parameter A_2 is still unknown since β is unknown. Therefore, a trial test is necessary.

In the trial test, an arbitrary value of A_2, denoted as A_2^{trial}, is defined. Then, by carrying out trial simulation, the relationship of crack growth rate, $(da/dN_L)^{\text{trial}}$ and SIFs range, ΔK^{trial}, is derived. By comparing with the Paris Law, the real value of A_2 can be determined, which is expressed as:

$$A_2 = A_2^{\text{trial}} \frac{(da/dN_L)}{(da/dN_L)^{\text{trial}}}. \tag{39}$$

Apart from PD fatigue model, the Paris Law can also be directly employed with the help of MCS criterion, which will be demonstrated in the following sections in detail.

3. Stress intensity factors

A_2 and m_2 in Eq. (32) are determined from the Paris law. As shown in Eq. (33), the SIF range plays an important role in fatigue analysis. SIFs describe the stress state in the vicinity of crack tips, which are commonly applied in the fracture analysis. J-integral method, proposed by Rice [41], is widely used by many researches in the literature [42-44] and previous works [45,46].

3.1. Interaction integral in peridynamics

A local coordinate system originated on crack tip is defined as shown in Fig. 5. To avoid the geometrical singularity, a closed form line contour is generated surrounding and away from the crack tip. However, since the formulation of the integral is in a line form, it is complicated in numerical simulation under PD framework. Hence, by using equivalent domain integral technique [47], J-integral in a domain form can be expressed as:

$$J = \int_A (\sigma_{kl} u_{k,1} - W\delta_{1l}) q_{,l} dA + \int_A (\sigma_{kl} u_{k,1} - W\delta_{1l})_{,l}\, q\, dA, \tag{40}$$

where W is the strain energy density. σ_{kl} is the stress in the local coordinate system. $u_{k,1}$ represents the spatial derivative along the x-axis in local coordinate system. A is the area enclosed by Γ_0, Γ and crack surfaces. q is a manually defined weight function as shown in Fig. 5. q equals to 1 at crack tip, while 0 on integral contour edge. r_{d} refers to the size of integral domain.

In this study, the q can be described as:

$$q = \begin{cases} 1 & \text{within } \Gamma_0 \\ (0,1) & \text{between } \Gamma_0 \text{ and } \Gamma \\ 0 & \text{outside } \Gamma \end{cases}. \tag{41}$$

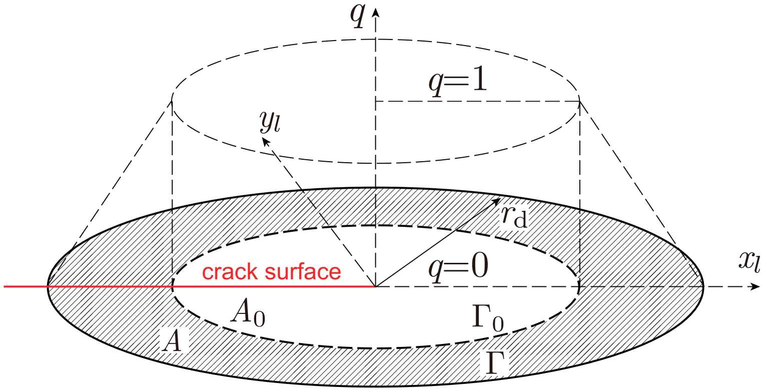

Figure 5: Layout of domain J-integral.

As one type of domain integral, interaction integral method defines an auxiliary field for stress and displacement fields, which is denoted as "aux". By superimposing (denoted as "sup") and decomposing the real and auxiliary fields, the interaction integral in static case can be expressed as:

$$I = \int_A \{(\sigma_{kl}^{\mathrm{aux}} u_{k,1} + \sigma_{kl} u_{k,1}^{\mathrm{aux}}) - \sigma_{km}^{\mathrm{aux}} \varepsilon_{km} \delta_{1l}\}\, q_{,l}\, dA + \int_A \rho \ddot{u}_k u_{k,1}^{\mathrm{aux}}\, q\, dA, \tag{42}$$

where ε_{km} represents the component of strain tensor. In Eq. (42), the first integral represents the static effect, while the second one refers to the dynamic effect. The stress and displacement fields can be derived directly from William's solution [48]. Finally, the mode-I and -II SIFs in the real field can be respectively extracted by:

$$K_\mathrm{I} = \frac{E^*}{2} I \quad (K_\mathrm{I}^{\mathrm{aux}} = 1,\; K_\mathrm{II}^{\mathrm{aux}} = 0), \tag{43a}$$

$$K_\mathrm{II} = \frac{E^*}{2} I \quad (K_\mathrm{I}^{\mathrm{aux}} = 0,\; K_\mathrm{II}^{\mathrm{aux}} = 1), \tag{43b}$$

where $K_\mathrm{I}^{\mathrm{aux}}$ and $K_\mathrm{II}^{\mathrm{aux}}$ are manually defined mode-I and -II SIFs in auxiliary field, respectively. Meanwhile, E^*=E is for plane stress assumption, while E^*=$E/(1-\nu^2)$ is for plane strain assumption.

3.2. Peridynamic differential operator

Eq. (42) is composed of several terms with spatial partial derivatives. There are many approaches to solve these PDEs, such as finite difference method [49,50] and moving least square method [43,51]. Alternatively, PDDO proposed by Madenci et al. [52] can be employed based on the framework of PD. PDDO is calculated based on the Taylor Series. In this study, the 2D second order Taylor Series is utilized as:

$$\begin{aligned} f(\boldsymbol{x}_j) = f(\boldsymbol{x}_i) + \xi_1 \frac{\partial f(\boldsymbol{x}_i)}{\partial x} + \xi_2 \frac{\partial f(\boldsymbol{x}_i)}{\partial y} + \frac{1}{2!}\xi_1^2 \frac{\partial^2 f(\boldsymbol{x}_i)}{\partial x^2} \\ + \frac{1}{2!}\xi_2^2 \frac{\partial^2 f(\boldsymbol{x}_i)}{\partial y^2} + \xi_1 \xi_2 \frac{\partial f(\boldsymbol{x}_i)}{\partial x \partial y} + R_0, \end{aligned} \tag{44}$$

where $f(\boldsymbol{x}_i)$ and $f(\boldsymbol{x}_j)$ refer to arbitrary physical parameters. ξ_1 and ξ_2 are the components of $\boldsymbol{\xi}$ along x- and y-coordinates. R_0 denote the remainder terms of the Taylor Series, which can be neglected.

By moving the first term on the right side to the left, multiplying each term with a PD function, $g_2^{p_1 p_2}(\boldsymbol{\xi})$, invoking the orthogonality property of the PD function, the PDEs can be transformed into spatial integral equation. The $g_2^{p_1 p_2}(\boldsymbol{\xi})$, as a key parameter in the PDDO, is determined by the shape functions in PD framework. Usually, the parameters with p_1+p_2=1 are used in the 1st order differentiation. For p_1+p_2=2, they are applied in the second order differentiation. For p_1+p_2=0, they are not considered. More detailed information can be found in [52] and previous works [45,46,53,54]. Therefore, the relationship between PDE and spatial integral equation up to second can be expressed as:

$$\begin{Bmatrix} \frac{\partial f(\boldsymbol{x}_i)}{\partial x} \\ \frac{\partial f(\boldsymbol{x}_i)}{\partial y} \\ \frac{\partial^2 f(\boldsymbol{x}_i)}{\partial x^2} \\ \frac{\partial^2 f(\boldsymbol{x}_i)}{\partial y^2} \\ \frac{\partial^2 f(\boldsymbol{x}_i)}{\partial x \partial y} \end{Bmatrix} = \int_{H_x} (f(\boldsymbol{x}_j) - f(\boldsymbol{x}_i)) \begin{Bmatrix} g_2^{10}(\boldsymbol{\xi}) \\ g_2^{01}(\boldsymbol{\xi}) \\ g_2^{20}(\boldsymbol{\xi}) \\ g_2^{02}(\boldsymbol{\xi}) \\ g_2^{11}(\boldsymbol{\xi}) \end{Bmatrix} dV. \tag{45}$$

In this article, the PD functions for the first order partial differential terms in 2D form is employed, which are given as:

$$g_2^{10}(\boldsymbol{\xi}) = \frac{2}{\pi h |\boldsymbol{\xi}| \delta^2} \cos\varphi, \quad g_2^{01}(\boldsymbol{\xi}) = \frac{2}{\pi h |\boldsymbol{\xi}| \delta^2} \sin\varphi. \tag{46}$$

3.3. Maximum circumferential stress criterion

Damages and cracks can automatically nucleate and propagate in PD by bond breaking. However, in order to examine the accuracy of the crack propagation, methods based on classical theory are also employed. Erdogan and Sih [35] proposed the MCS criterion. They believed that crack should propagate along the direction, where the circumferential stress reaches the maximum value. Therefore, the crack inclination angle, ϕ, is determined as:

$$\phi = 2\mathrm{arctan}\left(\frac{1}{4}\frac{K_{\mathrm{I}}}{K_{\mathrm{II}}} \pm \frac{1}{4}\sqrt{\left(\frac{K_{\mathrm{I}}}{K_{\mathrm{II}}}\right)^2 + 8}\right). \tag{47}$$

Meanwhile, the equivalent SIF, K_{eq}, can also be calculated based on the relationship between K_{I} and K_{II} as:

$$K_{\mathrm{eq}} = \frac{1}{4}\left(3\cos\frac{\phi}{2} + \cos\frac{3\phi}{2}\right)K_{\mathrm{I}} - \frac{3}{4}\left(\sin\frac{\phi}{2} + \sin\frac{3\phi}{2}\right)K_{\mathrm{II}}. \tag{48}$$

The SIFs can be calculated by interaction integral with the help of PDDO, and consequently, the ϕ and K_{eq} can also be determined. Substituting K_{eq} back to the ΔK in the Paris Law in Eq. (33), the magnitude of the fatigue crack growth in each cycle can be determined.

4. Numerical studies

Two mixed-mode fatigue failure analyses are presented. In Section 4.1, a 2D plate with pre-existing edged crack is studied. The fatigue crack growth and fatigue life will be evaluated in detail. In Section 4.2, the fatigue crack growth of root crack in a fillet welded joint is simulated. The crack paths calculated by PD fatigue model and MCS criterion are respectively investigated.

Since fatigue crack growth usually requires long time period, it can be regarded as a quasi-static problem. Different from ADR, the static calculation as described in Section 2.2 usually requires a good computing performance, since the stiffness matrix in Eq. (28) is large in size, especially for intermediate or refined discretization. However, the majority elements of the stiffness matrix are 0, and hence, the sparse matrix technique is employed to save computing resources and dramatically reduce the computing times. Therefore, for each cycle with new bond breakage, crack will propagate. Consequently, a static evaluation based on the new crack length is carried out. According to Section 2.3, the number of the cycles and the extreme values of bond stretch in each cycle are considered in the fatigue crack growth life prediction.

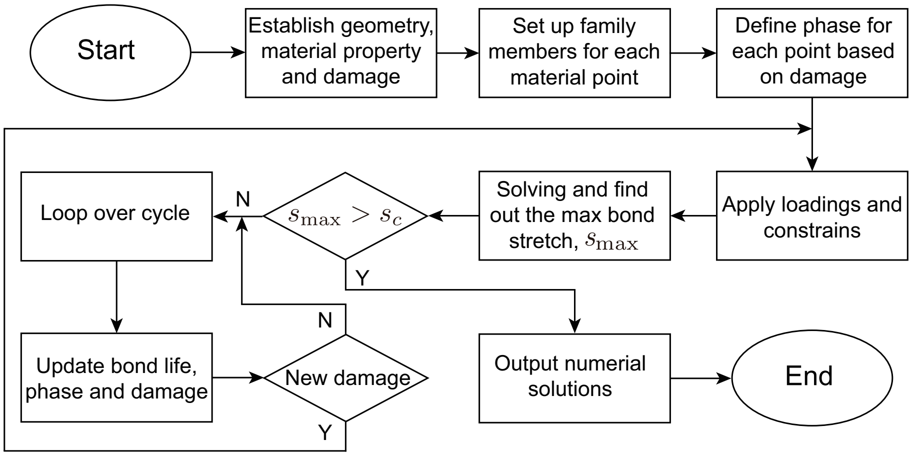

Figure 6: Flowchart of fatigue evaluation by OSPD.

The evaluation process can be described by a flowchart as shown in Fig. 6. For each cycle, it is necessary to judge whether to perform the fatigue analysis. Therefore, the maximum bond stretch, $s_{\max}$, are derived. If $s_{\max} \leq s_c$, the fatigue evaluation is conducted. The prediction of fatigue crack growth follows the procedures in Section 2.3 or 3.3. Once the bond breaks, new crack surface will emerge. Then, a static analysis based on current loadings and crack length are conducted. This process keeps going until $s_{\max} > s_c$. Then, the fatigue analysis will be terminated and fracture analysis on Phase III will be conducted.

4.1. Edged crack plate under mixed-mode tension

Sajith et al. [55] experimentally and numerically investigated the different fracture models by examining the fracture behaviour of 2D plate made by aluminium alloy 6061-T6 under mixed-mode loading conditions. The fitting parameters in Eq. (33), $\bar{C}$ and $\bar{m}$, are derived from the experiment tests, which are respectively given as 4.3378×10^{-7} (mm/cycle)/(MPa·m$^{0.5}$) and 2.6183. In this section, the crack propagation and fatigue life of this structure are reviewed by using PD.

The layout and geometry are presented as shown in Fig. 7. The elastic modulus and Poisson's ratio are 68 GPa and 0.33, respectively. Fracture toughness is 48.7 MPa$\sqrt{\mathrm{m}}$. The threshold strain is not considered and the plane stress assumption is applied. The maximum loading, $P_{\max}$, is 16 kN with loading angles of γ=45° and 60°, and the load ratio is defined as 0.1. The plate is fully fixed by the pins located on the lower region of the plate, while loadings are applied to the pins on the upper region. The pins on the plate can be regarded as rigid bodies. The loadings can be decomposed as:

$$P_1 = P_{\max}(0.5\cos\gamma + \sin\gamma), \tag{49a}$$

$$P_2 = -P_{\max}\sin\gamma, \tag{49b}$$

$$P_3 = P_{\max}(0.5\cos\gamma - \sin\gamma). \tag{49c}$$

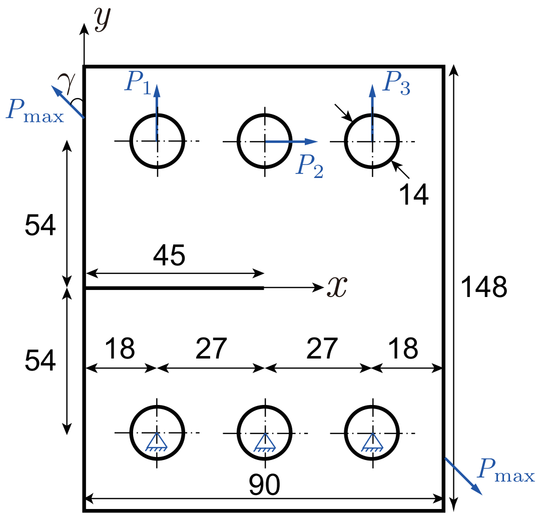

Figure 7: Layout and geometry of the plate with edged crack (unit: mm).

Before conducting the fatigue crack growth analysis, it is important to validate the accuracy of PD modelling. The crack opening displacements (COD) at maximum loading in the first cycle are provided in Fig. 8 with the FEM solutions calculated by ANSYS [56] as comparison. The PD model for each case is uniformly discretized by 180×296 material points, i.e., the grid spacing, Δx, equals to 0.5 mm. In order to add constraints on pins, the rows and columns of corresponding fixed points in the stiffness matrix and loading vector are removed, since the displacements of these points are already defined as 0. For FEM model, PLANE183 element is selected. Uniform mesh is applied on the majority of the plate, while for crack tip region, skewed mesh is utilized. There are total number of 14,868 elements and 45,079 nodes. Nodes at the centre of lower pins are fully constrained, while at the centre of top pins are subjected to loadings. As shown in Fig. 8, for both cases, the COD in x- and y-direction by PD are matched well with those by FEM. Hence, the crack patterns are also the same.

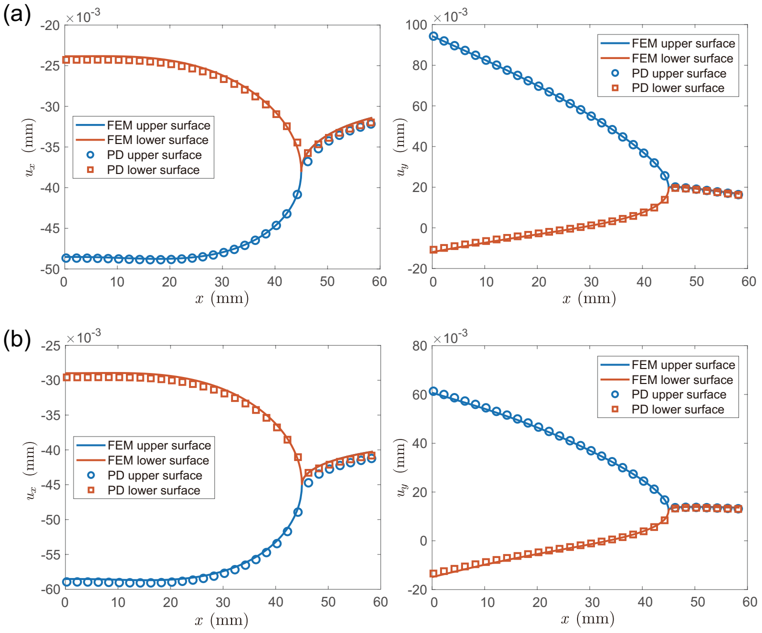

Figure 8: COD comparisons: (a) u_x and u_y at γ=45°, (b) u_x and u_y at γ=60°.

The mode-I and -II SIFs are also provided in Table 1. As the loading angle increase, the K_{I} decreases, while the K_{II} increases. For both cases, the values of K_{I} and K_{II} by OSPD have good agreements with FEM. The maximum differences between OSPD and FEM solutions are below 1%. Meanwhile, the path independency can be accomplished. Both COD and SIFs results has proved the accuracy of OSPD. Then the fatigue crack growth is evaluated.

The S-N curve and Paris Law diagram can be derived for the literature [55,57]. Therefore, the values of A_1, m_1 and m_2 can be calculated as, 103.75, 2.2915 and 2.6183, respectively. However A_2 can not be derived directly, and a trial test is necessary as mentioned in Section 2.3. A_2^{trial} is randomly defined as 2,000. In considering the Eq. (39) and following the procedure shown in Fig. 6, the real value of A_2 is determined as 1,066. Fig. 9 and Fig.

Table 1: Mixed-mode SIFs by OSPD for edge-cracked plate (unit: MPa$\sqrt{\text{m}}$).

	45°		60°	
r_d	K_I	K_II	K_I	K_II
$30\Delta x$	8.7891	-4.4533	6.2083	-5.3770
$45\Delta x$	8.8440	-4.4716	6.2470	-5.4002
$60\Delta x$	8.8715	-4.4799	6.2664	-5.4107
FEM	8.7883	-4.4580	6.2051	-5.3824

10 show the predicted fatigue life and crack propagation path of the pinned plate under loadings, respectively. Results are compared with experimental data from [55].

For each cycle, position of the crack tip should be recorded. A crack length increment is the distance of crack tips between N_L and N_L+1 cycles. By integrating of the crack length increments in each cycle, the variation of crack length can be determined. Then, the comparisons in crack length between experiment and PD are shown in Fig. 9. The relatively large A_2^{trial} gives an over-estimation in the reduction of bond remaining life, leading to a short life cycles. After modification of A_2 based on experimental data, the prediction from OSPD matches well with experiments in both loading cases. The predicted crack propagation paths under different loadings are provided in Fig. 10. The crack growth predictions determined by PD fatigue model and PD MCS criterion are compared with the experiment data, meanwhile, a novel energy-based criteria for PD fatigue model proposed by Nguyen et al. [28], is also employed for comparison. Relatively good agreements between the experiment data and numerical solutions can be obtained.

4.2. Fatigue crack growth of a root crack in a fillet welded joint

To further evaluate the capability of PD fatigue model, fatigue crack growth of a root crack in a welded joint structure is analysed. The main layout and geometry of the welded joint cross section are provided as shown in Fig. 11 [58]. It is assumed that the structure is also made of same material in previous example from [55]. Uniform stress loadings, σ_{11} and σ_{22} are subjected to the far ends of the joint. σ_{22} is defined as 50 MPa. The ratios of applied stresses, σ_{11}/σ_{22}, are set as -1, 0, 1, respectively. Meanwhile, the plane stress assumption is employed. For better comparisons of the numerical solutions, the normalized SIFs are employed, which can be expressed as $\bar{K}_i$=$K_i/(\sigma_{22}\sqrt{\pi a})$, in which i=I, II. a refers to crack length.

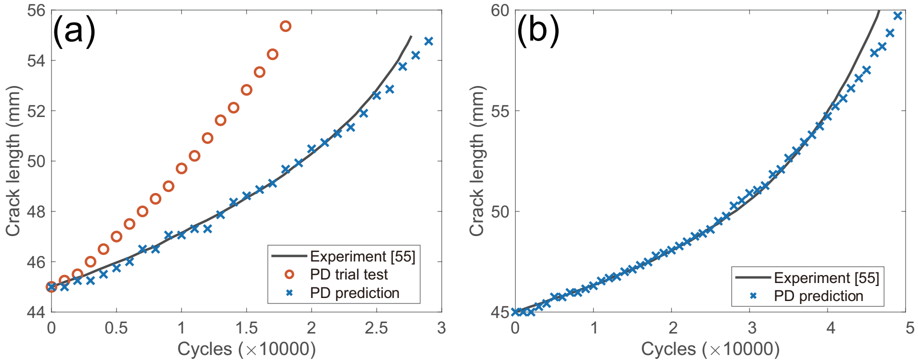

Figure 9: Prediction of fatigue crack growth life: (a) γ=45°, (b) γ=60°.

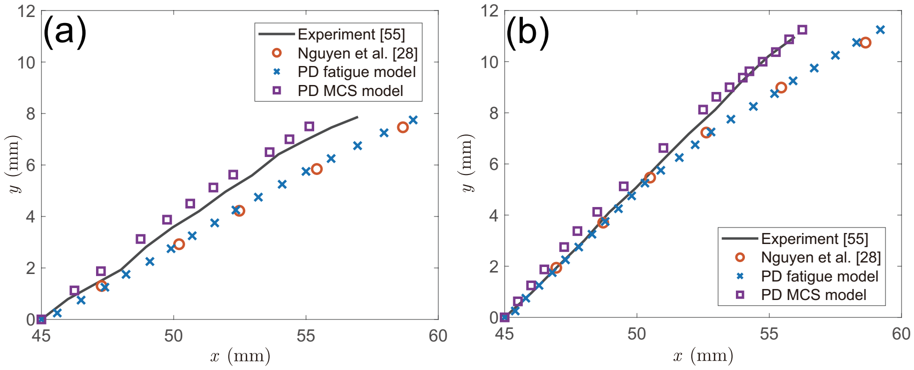

Figure 10: Crack propagation path: (a) γ=45°, (b) γ=60°.

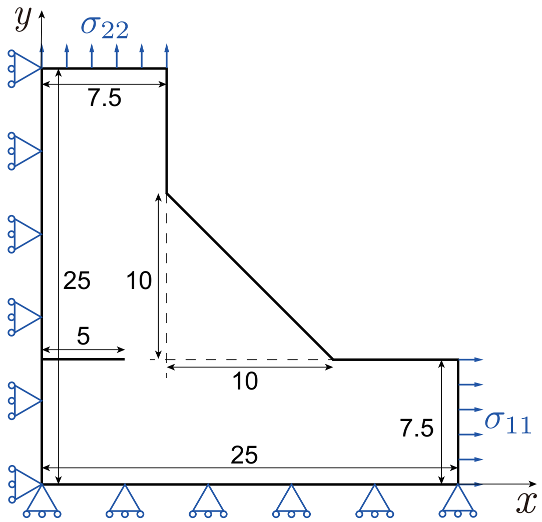

Figure 11: Layout and geometry of a weld joint structure (unit: mm).

Since the experimental data are not available in the literature, the PD parameter, A_1 and m_1, can not be determined. Moreover, the prediction of fatigue life can not be provided either. However, as shown in Eq. (32), the decrease of bond remaining life is proportional to the exponent of cyclic bond stretch. It controls the speed of remaining life decay, but it will not affect the direction of fatigue crack growth. Therefore, in this section, only crack propagation under different loading ratios are evaluated in detail.

The weld joint structure is uniformly discretized by points with a grid spacing of Δx=0.1 mm. Since the bottom and left edges are symmetric surfaces as shown in Fig. 11, two fictitious regions with three layer of points are employed to represent boundary constraints. Therefore, the number of the points is 36,925 in real region and 1,500 in fictitious region, respectively.

Fig. 12 shows the COD results in the initial state of fatigue analysis comparing with FEM produced by ANSYS [56]. The PD solution and FEM solutions match well in CODs along y-direction for all loading conditions. However, the solutions of CODs along x-direction are slightly different at crack tip region, which may be due to the non-local property of PD. The magnitude of displacements in front of the crack tip might be affected by those behind the crack tip. As a consequence, the K_{I} values between two methods agree well with each other, while there are differences in K_{II} values

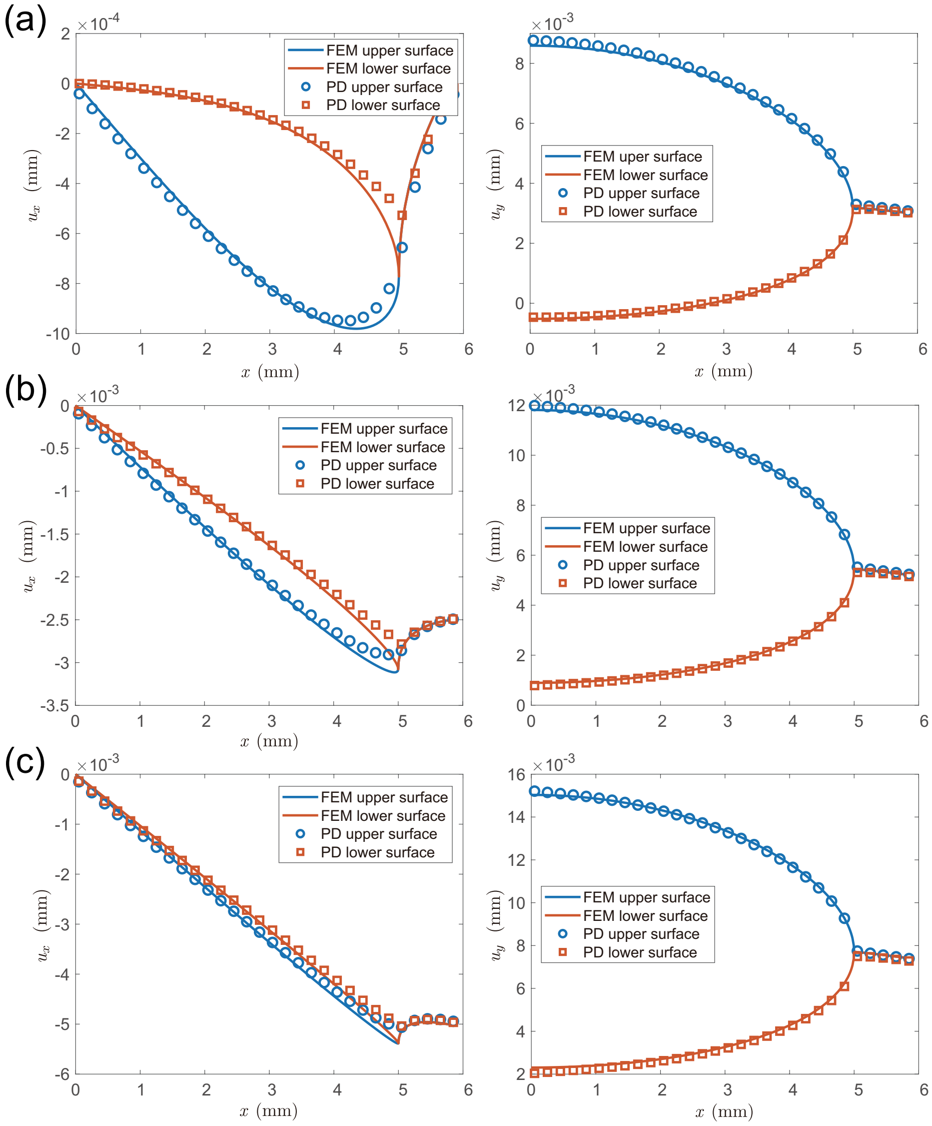

Figure 12: COD comparison of welded joint under different loading conditions at initial state: (a) u_x and u_y at σ_{11}/σ_{22}=1, (b) u_x and u_y at σ_{11}/σ_{22}=0, (c) u_x and u_x at σ_{11}/σ_{22}=-1.

as shown in Table 2, which might due to the small values of the reference K_{II}. As the decrease of σ_{11}/σ_{22}, the sliding between upper and lower surfaces gradually diminish. Therefore, the loadings on the weld toe change from mixed-mode condition to mode-I condition.

Table 2: Normalized mixed-mode SIFs comparison for weld joint.

σ_{11}/σ_{22}	1		0		-1	
	$\bar{K}_{\text{I}}$	$\bar{K}_{\text{II}}$	$\bar{K}_{\text{I}}$	$\bar{K}_{\text{II}}$	$\bar{K}_{\text{I}}$	$\bar{K}_{\text{II}}$
PD	0.6116	-0.0959	0.7285	-0.0663	0.8453	-0.0368
FEM	0.6080	-0.0941	0.7270	-0.0639	0.8460	-0.0336
RKPM [58]	0.6073	-0.0939	0.7259	-0.0636	0.8450	-0.0331

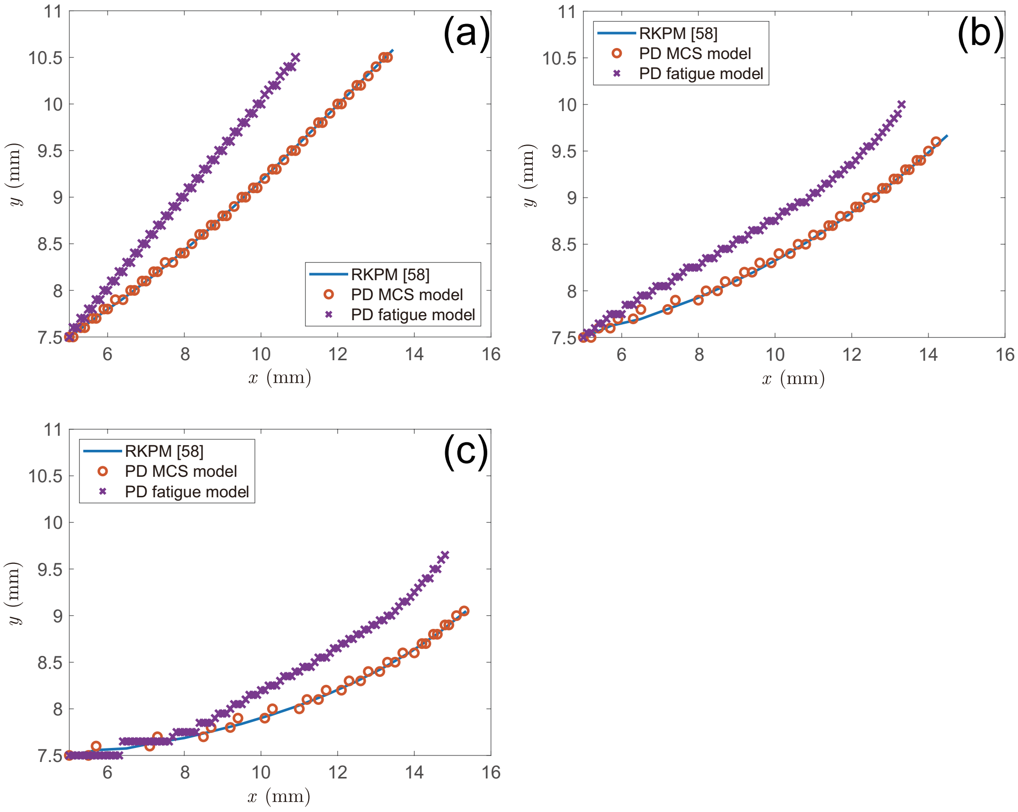

Figure 13: Crack path comparison by different numerical methods under different loading conditions: (a) σ_{11}/σ_{22}=1, (b) σ_{11}/σ_{22}=0, (c) σ_{11}/σ_{22}=-1.

The crack growth in the weld toe structure under different loading conditions is provided in Fig. 13. As σ_{11}/σ_{22} changes from 1 to -1, the crack inclination angle decreases correspondingly, which is due to the decrease of the mode-II influence based on Eq. (47). Reference solutions [58] produced by RKPM, which were well validated by extended FEM, are also provided. Numerical solutions calculated by MCS criterion have good agreements with the reference solutions in all loading conditions. However, there are gaps between PD predictions and reference solutions. Moreover, the magnitude of the differences increases as the mode-II influence increases.

4.3. Discussion

The accuracy of numerical solutions about the crack path and fatigue life predictions in pure mode-I were well proved in [28]. However, it may not always give good predictions in the mixed-mode fatigue crack growth path. One of the possible reasons might be the COD disturbance around the crack tip as shown in Fig. 12, which leads to a different crack pattern as compared with FEM solutions, and hence, the core bond might change. Another possible reason might be the mode-I assumption in PD fatigue model. As shown in Fig. 4, the core bonds perpendicular to the crack surface are assumed to be failed during cyclic loading. However, in mixed-mode loading conditions, these bonds might not have the maximum stretch. Instead, some slant bonds will firstly reach the maximum stretch state and then break, as shown in Fig. 14.

Meanwhile, in the framework of PD, the crack extension does not directly determined by the stress intensity around the crack tip. The stress state in the vicinity of the crack tip region is usually reflected by the different extent of bond stretches. Due to the bond distribution around the crack tip, there may not have enough options for cracks to propagate.

As shown in Fig. 14, the broken bond in the cases of σ_{11}/σ_{22}=0 and 1 are the same at the initial crack growth stage. Therefore, if the direction of broken bonds match with the direction by MCS criterion, the PD will give relatively accurate prediction as shown in Section 4.1. Otherwise, there might be a difference between PD crack growth and reference solutions. Hence, as shown in Fig. 13, for σ_{11}/σ_{22}=0 and 1, the crack growth direction differs with the reference solutions in the initial stages. For σ_{11}/σ_{22}=-1, since the initial stage is a mode-I dominant loading condition, the crack growth calculated by PD matches with those by MCS and RKPM. As the further growth of crack, the mode-II influence becomes evident, and then the crack path gradually differs with the reference solutions.

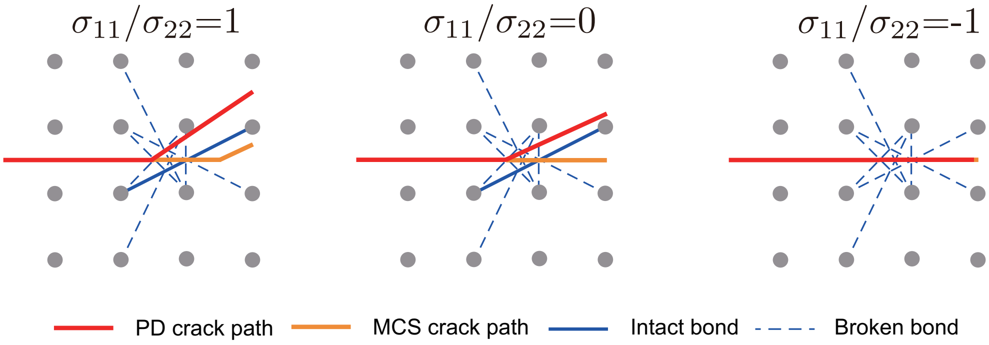

Figure 14: Fatigue crack growth at initial stage.

The MCS criterion utilized in this study have a relatively good estimation of crack growth path. However, the prediction of fatigue life might not always be accurate due to the relative large integral contour during the calculation of SIFs. Moreover, as a classical method in fracture analysis, MCS criterion might have difficulties in the simulations of some complex fracture behaviours, such as crack branching.

Overall, the PD fatigue model use trial and real processes to simulate the fatigue crack growth with certain extent accuracy. By distinguishing Phases I and II, the fatigue crack nucleation and propagation are well presented. Both original fatigue model and MCS criterion are based on PD framework. Hence, the crack propagation can be automatically calculated and predicted without re-meshing and any further manual intervention as commonly applied in classical methods. Meanwhile, since the new damage still relies on the bond breakage, the main logic of predicting crack nucleation and propagation does not change. Therefore, the fatigue analysis can be directly switched to fast crack growth analysis (Phase III) without further modification. It reduces the complexity and increases the efficiency of numerical calculation. The non-local MCS criterion can be employed to aid the crack propagation path prediction by PD.

5. Conclusion

In this study, performance of PD fatigue model in the mixed-mode fracture analysis is evaluated in detail. The fatigue crack growth is assumed as a quasi-static process. Therefore, to determine the displacement field in each crack increment, the static formulation is introduced. The meshfree interaction integral method is employed to calculate the SIFs. The PDDO is utilized to transform the PDE in the equation of interaction integral into corresponding spatial integral form. Moreover, the non-local MCS criterion based on PD framework is also tested as comparison.

Two numerical methods are implemented in the fatigue crack growth analysis. First, a pinned plate with edged crack made by aluminium alloy is studied. The crack growth paths and fatigue lives for different loadings are compared and discussed. Secondly, a welded joint structure with a root crack under different loadings are investigated. Only crack growth paths are compared due to the limitations of experimental data. To sum up, the PD fatigue model and the non-local MCS criterion have their own merits and drawbacks in the mixed-mode fatigue failure analysis. Hence, in the future studies, it is of vital importance to improve the numerical accuracy of the PD fatigue model in the fracture analysis. This study have given non-local meshfree solutions for the fatigue failure analysis, which might provide theoretical supports for the engineering applications.

References

[1] C. Erny, D. Thevenet, J.Y. Cognard, M. Körner, Fatigue life prediction of welded ship details, Mar. Struct. 25 (2012) 13-32. https://doi.org/10.1016/j.marstruc.2011.10.001.

[2] W. Fricke, Fatigue analysis of welded joints: state of development, Mar. Struct. 16 (2003) 185-200. https://doi.org/10.1016/S0951-8339(02)00075-8.

[3] P.C. Paris, M.P. Gomez, W.E. Anderson, A rational analytic theory of fatigue, Trends Eng. 13 (1961) 9-14.

[4] M. Sander, H.A. Richard, Experimental and numerical investigations on the influence of the loading direction on the fatigue crack growth, Int. J. Fatigue 28 (2006) 583-591. https://doi.org/10.1016/j.ijfatigue.2005.05.012.

[5] O. Nguyen, E.A. Repetto, M. Ortiz, R.A. Radovitzky, A cohesive model of fatigue crack growth, Int. J. Fract. 110 (2001) 351-369. https://doi.org/10.1023/A:1010839522926.

[6] A.M. Yan, H. Nguyen-Dang, Multiple-cracked fatigue crack growth by BEM, Comput. Mech. 16 (1995) 273-280. https://doi.org/10.1007/BF00350716.

[7] I.V. Singh, B.K. Mishra, S. Bhattacharya, R.U. Patil, The numerical simulation of fatigue crack growth using extended finite element method, Int. J. Fatigue 36 (2012) 109-119. https://doi.org/10.1016/j.ijfatigue.2011.08.010.

[8] G. Scetta, N. Selles, P. Heuillet, M. Ciccotti, C. Creton, Cyclic fatigue failure of TPU using a crack propagation approach, Polym. Test. 97 (2021) 107140. https://doi.org/10.1016/j.polymertesting.2021.107140.

[9] S. Ye, C.C. Zhang, P.Y. Zhang, X.C. Zhang, S.T. Tu, R.Z. Wang, Fatigue life prediction of nickel-based GH4169 alloy on the basis of a multi-scale crack propagation approach, Eng. Fract. Mech. 199 (2018) 29-40. https://doi.org/10.1016/j.engfracmech.2018.05.023.

[10] K. Yagi, S. Tanaka, T. Kawahara, K. Nihei, H. Okada, N. Osawa, Evaluation of crack propagation behaviors in a T-shaped tubular joint employing tetrahedral FE modeling, Int. J. Fatigue 96 (2017) 270-282. https://doi.org/10.1016/j.ijfatigue.2016.11.028.

[11] A. Grbovic, B. Rasuo, FEM based fatigue crack growth predictions for spar of light aircraft under variable amplitude loading, Eng. Fract. Mech. 26 (2012) 50-64. https://doi.org/10.1016/j.engfailanal.2012.07.003.

[12] R. Branco, F.V. Antunes, J.D. Costa, A review on 3D-FE adaptive remeshing techniques for crack growth modelling, Eng. Fract. Mech. 141 (2015) 170-195. https://doi.org/10.1016/j.engfracmech.2015.05.023.

[13] T.N. Bittencourt, P.A. Wawrzynek, A.R. Ingraffea, J.L. Sousa, Quasi-automatic simulation of crack propagation for 2D LEFM problems, Eng. Fract. Mech. 55 (1996) 321-334. https://doi.org/10.1016/0013-7944(95)00247-2.

[14] M. Duflot, H. Nguyen-Dang, Fatigue crack growth analysis by an enriched meshless method, J. Comput. Appl. Math. 168 (2004) 155-164. https://doi.org/10.1002/nme.948.

[15] A. Jameel, G.A. Harmain, Fatigue crack growth in presence of material discontinuities by EFGM, Int. J. Fatigue 81 (2015) 105-116. https://doi.org/10.1016/j.ijfatigue.2015.07.021.

[16] T. Belytscho, Y.Y. Lu, L. Gu, Element-free Galerkin methods, Int. J. Numer. Methods Eng. 37 (1994) 229-256. https://doi.org/10.1002/nme.1620370205.

[17] H. Pathak, A. Singh, I.V. Singh, Numerical simulation of 3D thermo-elastic fatigue crack growth problems using coupled FE-EFG approach, J. Inst. Eng. India Ser. C. 98 (2017) 295-312. https://doi.org/10.1007/s40032-016-0256-7.

[18] M.J. Dai, S. Tanaka, S. Sadamoto, T. Yu, T.Q. Bui, Advanced reproducing kernel meshfree modeling of cracked curved shells for mixed-mode stress resultant intensity factors, Eng. Fract. Mech. 233 (2020) 107012. https://doi.org/10.1016/j.engfracmech.2020.107012.

[19] W.K. Liu, S. Jun, Y.F. Zhang, Reproducing kernel particle methods, Int. J. Numer. Methods Fluids 20 (1995) 1081-1106. https://doi.org/10.1002/fld.1650200824.

[20] S. Tanaka, H. Suzuki, S. Sadamoto, M. Imachi, T.Q. Bui, Analysis of cracked shear deformable plates by an effective meshfree plate formulation. Eng. Fract. Mech. 144 (2015) 142-157. https://doi.org/10.1016/j.engfracmech.2015.06.084.

[21] S. Tanaka, H. Suzuki, S. Sadamoto, S. Sannomaru, T. Yu, T.Q. Bui, J-integral evaluation for 2D mixed-mode crack problems employing a meshfree stabilized conforming nodal integration method. Comput. Mech. 58 (2016) 185-198. https://doi.org/10.1007/s00466-016-1288-9.

[22] S.A. Silling, Reformulation of elasticity theory for discontinuities and long-range forces, J. Mech. Phys. Solids 48 (2000) 175-209. https://doi.org/10.1016/S0022-5096(99)00029-0.

[23] M. Imachi, S. Tanaka, T.Q. Bui, S. Oterkus, E. Oterkus, A computational approach based on ordinary state-based peridynamics with new transition bond for dynamic fracture analysis, Eng. Fract. Mech. 206 (2019) 359-374. https://doi.org/10.1016/j.engfracmech.2018.11.054.

[24] H.A. Nguyen, H. Wang, S. Tanaka, S. Oterkus, E. Oterkus, An in-depth investigation of bimaterial interface modeling using ordinary state-based peridynamics, J. Peridyn. Nonlocal Model. 4 (2022) 112-138. https://doi.org/10.1007/s42102-021-00058-x.

[25] E. Oterkus, I. Guven, E. Madenci, Fatigue failure model with peridynamic theory, In 2010 12th IEEE Intersociety Conference on Thermal and Thermomechanical Phenomena in Electronic Systems, Las Vegas, NV, USA (2010) 1-6. https://doi.org/10.1109/ITHERM.2010.5501273.

[26] S.A. Silling, A. Askari, Peridynamic model for fatigue cracking, Sandia National Lab, 2014, Report No. SAND2014-18590. https://doi.org/10.2172/1160289.

[27] P. Paris, F. Erdogan, A critical analysis of crack propagation laws, ASME. J. Basic Eng. 85 (1963) 528-533. https://doi.org/10.1115/1.3656900.

[28] C.T. Nguyen, S. Oterkus, E. Oterkus, An energy-based peridynamic model for fatigue cracking, Eng. Fract. Mech. 241 (2021) 107373. https://doi.org/10.1016/j.engfracmech.2020.107373.

[29] J. Jung, J. Seok, Mixed-mode fatigue crack growth analysis using peridynamic approach. Int. J. Fatigue 103 (2017) 591-603. https://doi.org/10.1016/j.ijfatigue.2017.06.008.

[30] J. Jung, J. Seok, Fatigue crack growth analysis in layered heterogeneous material systems using peridynamic approach. Compos. Struct. 152 (2016) 403-407. https://doi.org/10.1016/j.compstruct.2016.05.077.

[31] O. Karpenko, S. Oterkus, E. Oterkus, Peridynamic analysis to investigate the influence of microstructure and porosity on fatigue crack propagation in additively manufactured Ti6Al4V, Eng. Fract. Mech. 261 (2022) 108212. https://doi.org/10.1016/j.engfracmech.2021.108212.

[32] N. Zhu, C. Kochan, E. Oterkus, S. Oterkus, Fatigue analysis of polycrystalline materials using Peridynamic Theory with a novel crack tip detection algorithm, Ocean Eng. 222 (2021) 108572. https://doi.org/10.1016/j.oceaneng.2021.108572.

[33] K. Hong, S. Oterkus, E. Oterkus, Peridynamic analysis of fatigue crack growth in fillet welded joints, Ocean Eng. 235 (2021) 109348. https://doi.org/10.1016/j.oceaneng.2021.109348.

[34] J.F. Yau, S.S. Wang, H.T. Corten, A mixed-mode crack analysis of isotropic solid using conservation laws of elasticity, ASME. J. Appl. Mech. 47 (1980) 335-341. https://doi.org/10.1115/1.3153665.

[35] F. Erdogan, G.C. Sih, On the crack extension in plates under plane loading and transverse shear, ASME. J. Basic Eng. 85 (1963) 519-525. https://doi.org/10.1115/1.3656897.

[36] S.A. Silling, E. Askari, A meshfree method based on the peridynamic model of solid mechanics, Comput. Struct. 83 (2005) 1526-1535. https://doi.org/10.1016/j.compstruc.2004.11.026.

[37] S.A. Silling, M. Epton, O. Weckner, J. Xu, E. Askari, Peridynamic states and constitutive modeling, J. Elasticity 88 (2007) 151-184. https://doi.org/10.1007/s10659-007-9125-1.

[38] E. Madenci, E. Oterkus, Peridynamic theory and its applications, Springer, New York, 2014. https://doi.org/10.1007/978-1-4614-8465-3.

[39] B. Kilic, E. Madenci, An adaptive dynamic relaxation method for quasi-static simulations using the peridynamic theory, Theor. Appl. Fract. Mech. 53 (2010) 194-204. https://doi.org/10.1016/j.tafmec.2010.08.001.

[40] P. Underwood, Dynamic Relaxation, in: T. Belytschko, T.J.R. Hughes (Eds.), Computational Methods for Transient Analysis, North-Holland, Amsterdam, 1983, pp.245-265.

[41] J.R. Rice, A path independent integral and the approximate analysis of strain concentration by notches and cracks, ASME. J. Appl. Mech. 35 (1968) 379-386. https://doi.org/10.1115/1.3601206.

[42] S.H. Song, G.H. Paulino, Dynamic stress intensity factors for homogeneous and smoothly heterogeneous materials using the interaction integral method, Int. J. of Solids Struct. 43 (2006) 4830-4866. https://doi.org/10.1016/j.ijsolstr.2005.06.102.

[43] M. Imachi, S. Tanaka, T.Q. Bui, Mixed-mode dynamic stress intensity factors evaluation using ordinary state-based peridynamics, Theor. Appl. Fract. Mech. 93 (2018) 97-104. https://doi.org/10.1016/j.tafmec.2017.07.008.

[44] M.J. Dai, S. Tanaka, S. Oterkus, E. Oterkus, Mixed-mode stress intensity factors evaluation of flat shells under in-plane loading employing ordinary state-based peridynamics, Theor. Appl. Fract. Mech. 112 (2021) 102841. https://doi.org/10.1016/j.tafmec.2020.102841.

[45] H. Wang, S. Tanaka, S. Oterkus, E. Oterkus, Evaluation of stress intensity factors under thermal effect employing domain integral method and ordinary state based peridynamic theory, Continuum Mech. Thermodyn. (2021). https://doi.org/10.1007/s00161-021-01033-z.

[46] H. Wang, S. Tanaka, S. Oterkus, E. Oterkus, Fracture parameter investigations of functionally graded materials by using ordinary state based peridynamics, Eng. Anal. Bound. Elem. 139 (2022) 180-191. https://doi.org/10.1016/j.enganabound.2022.03.005.

[47] I.S. Raju, K.N. Shivakumar, An equivalent domain integral method in the two-dimensional analysis of mixed mode crack problems, Eng. Fract. Mech. 37 (1990) 707-725. https://doi.org/10.1016/0013-7944(90)90070-W.

[48] M.L. William, On the stress distribution at the base of a stationary crack, ASME. J. Appl. Mech. 24 (1957) 109-114. https://doi.org/10.1115/1.4011454.

[49] J.C. Strikwerda, Finite difference schemes and partial differential equations, second ed., SIAM, Philadelphia, 2004. https://doi.org/10.1137/1.9780898717938.

[50] R.J. LeVeque, Finite difference methods for ordinary and partial differential equations: steady-state and time-dependent problems, SIAM, Philadelphia, 2007. https://doi.org/10.1137/1.9780898717839.

[51] M. Imachi, S. Tanaka, M. Ozdemir, T.Q. Bui, S. Oterkus, E. Oterkus, Dynamic crack arrest analysis by ordinary state-based peridynamics, Int. J. Fract. 221 (2020) 155-169. https://doi.org/10.1007/s10704-019-00416-3.

[52] E. Madenci, A. Barut, M. Futch, Peridynamic differential operator and its applications, Comput. Methods Appl. Mech. Eng. 304 (2016) 408-451. https://doi.org/10.1016/j.cma.2016.02.028.

[53] H. Wang, E. Oterkus, S. Oterkus, Predicting fracture evolution during lithiation process using peridynamics, Eng. Fract. Mech. 192 (2018) 176-191. https://doi.org/10.1016/j.engfracmech.2018.02.009.

[54] H. Wang, E. Oterkus, S. Oterkus, Three-dimensional peridynamic model for predicting fracture evolution during the lithiation process, Energies 11 (2018) 1461. https://doi.org/10.3390/en11061461.

[55] S. Sajith, K.S.R.K. Murthy, P.S. Robi, Experimental and numerical investigation of mixed mode fatigue crack growth models in aluminum 6061-T6, Int. J. Fatigue 130 (2020) 105285. https://doi.org/10.1016/j.ijfatigue.2019.105285.

[56] Ansys Mechanical APDL Verification Manual (2021), VM267:Inclined cracked in 2-D plate under uniform tension loading. 757-758.

[57] R.R. McCullough, J.B. Jordon, P.G. Allison, T. Rushing, L. Garcia, Fatigue crack nucleation and small crack growth in an extruded 6061 aluminum alloy. Int. J. Fatigue 119 (2019) 52-61. https://doi.org/10.1016/j.ijfatigue.2018.09.023.

[58] S. Tanaka, A. Takata, M.J. Dai, H. Wang, S. Sadamoto, Fracture analysis employing equivalent domain integral method and nodal integration techniques based on reproducing kernel particle method, Comput. Part. Mech. 9 (2022) 1265-1278. https://doi.org/10.1007/s40571-022-00458-w.